Energy Advances

ROYAL SOCIETY OF CHEMISTRY

PAPER

View Article Online
View Journal

Cite this: DOI: 10.1039/d5ya00266d

Molten salt assisted synthesis of a lignin derived porous carbon host for lithium–sulfur battery cathodes

Juhana Jämsén, *[a] Pauliina Nevalainen,[b] Kirill Murashko[a] and Anna Lähde[a]

Received 12th September 2025,
Accepted 29th November 2025

DOI: 10.1039/d5ya00266d

rsc.li/energy-advances

Lithium–sulfur batteries offer high theoretical energy density and low cost. However, challenges such as the polysulfide shuttle effect and poor conductivity of sulfur have hindered their commercial application. In this work, porous nitrogen-doped carbon materials were synthesized from Kraft lignin using a molten salt method combined with urea and K_2CO_3 for pore generation in a single synthesis step. The use of a KCl/NaCl salt mixture as the reaction medium allowed for control over product morphology and increased yield by retaining volatiles. The effects of varying lignin/urea/K_2CO_3 mass ratios on the characteristics of the produced materials were analyzed. The carbon-based host materials were then combined with sulfur through chemical deposition and melt diffusion. The properties of the host materials and composites were characterized using TGA, SEM, EDS, BET, XPS, and Raman analyses. Electrochemical tests were conducted to study the impact on the electrochemical properties of the lithium–sulfur battery cathode. The analysis revealed that the controlled porosity and functionalization of the host materials significantly influence the distribution and utilization of sulfur during electrochemical testing. By analyzing the effects of host material porosity and nitrogen doping, we improved the electrochemical properties of the cathode material. The best performing composite material exhibited a high initial discharge capacity 1407 mAh per g-S (83% of the theoretical capacity of sulfur) and retained 825 mAh g^{-1} capacity (average fade of 0.105% per cycle) and 98.7% coulombic efficiency after 200 cycles. In addition, the material displayed good performance at commercially viable mass loading.

1. Introduction

Concerns over environmental change and the urgent need for sustainable energy solutions have driven increased interest in energy storage technologies. The intermittent nature of renewable energy sources requires wide-scale electrical energy storage, while lithium-ion batteries struggle to fulfill all the demands of current society.[1] In 2023, the total battery capacity produced was 2.5 TWh, and it is estimated to exceed 9 TWh by 2030. In the case of electric vehicle batteries, demand is estimated to increase over tenfold by 2035 compared to 2023.[2] The high cost of batteries remains a significant inhibitor to EV adoption globally.[3,4] Additionally, the availability of critical elements causes economic, environmental, and geopolitical concerns.[5] Therefore, enhancing the environmental sustainability of the battery value chain while reducing costs is crucial.

The lithium–sulfur battery, first introduced in the 1960s, offers a high theoretical capacity of 1670 mAh g^{-1} and a theoretical energy density of up to 2600 Wh kg^{-1}.[6,7] Other benefits include the affordable price and wide availability of sulfur, as well as excellent mechanical properties, safety, and sustainability.[8–10] Potential and current applications for lithium–sulfur batteries include heavy electric vehicles, aerospace, aviation, and maritime applications.[10] However, several challenges have impeded their commercial application, including the lithium polysulfide (LiPS) shuttle effect, lithium dendrite growth, low conductivity of sulfur and large volume expansion upon formation of Li_2S.[9,11–13] The aforementioned disadvantages were mitigated to a certain extent by the incorporation of mesoporous carbon as a sulfur host in 2009 resulting in a resurgence of research interest.[6]

Since then, a variety of carbon materials have been explored as cathode composites with sulfur, including carbon nanotubes, graphene, carbon nanofibers, and porous carbon. Among these, porous carbon is a popular choice due to its high conductivity, large surface area, and affordable price.[10] Porous carbon can suppress the shuttling effect and facilitate volume changes during the cycle.[14] Micropores prevent long-chain LiPS diffusion while

[a] University of Eastern Finland, Department of Biological and Environmental Sciences, Yliopistonranta 8, 70210, Kuopio, Finland. E-mail: juhana.jamsen@uef.fi
[b] University of Eastern Finland, Department of Chemistry and Sustainable Technology, Yliopistokatu 2, 80100, Joensuu, Finland

mesopores provide room for sufficient sulfur loading, pathways for Li-ion transport and adequate contact with the electrolyte.[10] In order to combine these benefits, hierarchical porous carbons containing both micro and mesopores have been investigated.[14] In general, porous carbon is produced by one of two pathways: physical activation by reactive gases or chemical activation with the aid of pore-inducing reagents.[15] Diverse biomass sources can be used as feedstock for producing porous carbon, resulting in high porosity, large specific surface area, high chemical stability, high electrical conductivity, and desirable mechanical properties.[16]

Among all biomasses, lignin stands out as a suitable choice for porous carbon creation as it is the second most abundant biopolymer, making it renewable and cost-effective. Despite its apparent potential, only 2% of the 70 million tons produced by paper mills and biorefineries annually is utilized in high-value use.[17] Therefore, the use of lignin-based materials in energy storage applications has been extensively reviewed in recent years.[18–22] Lignin use has been reported in cathode material, binder, and separator coating in lithium–sulfur batteries.[23–25] It has been demonstrated that type and source of lignin result in varying multiscale and electrochemical properties in activated carbon.[26–28] Use of Kraft lignin results in higher oxygen content, while use of hardwood lignin results in higher specific surface area (SSA) and porosity.[29,30] In order to enhance the performance of lignin-based carbon materials, the implementation of heteroatom doping has been proposed.[31–34] Both N and O doping notably enhance the interactions between the carbon host and LiPs.[31] Oxygen functional groups contribute to cathode performance by sulfur adsorption and suppressing migration and localization of S-species during cycling.[35,36] Doping cathode material with nitrogen at suitable levels (4–8%) can improve cycle life, sulfur utilization, conductivity and assist in combating the polysulfide shuttle.[37,38] Nitrogen-doping of mesoporous carbon cathode material has been shown to improve electrochemical performance, with pyridinic nitrogen providing the most pronounced effect.[39,40] Nitrogen doping of the carbon material is typically achieved by either the use of a nitrogen-containing precursor in pyrolysis or post-treatment with a nitrogen-containing agent.[41]

Using a mixture of urea and potassium carbonate for the activation of lignin has been found to greatly increase the surface area and volume of the produced material compared to using only potassium carbonate. This approach has enabled the synthesis of nitrogen-doped micro-mesoporous carbon with BET surface area of up to 3400 $m^2\ g^{-1}$ and a total pore volume of up to 2.3 $cm^3\ g^{-1}$.[42] Similar results have been achieved by using KOH and melamine.[43,44] This approach has been reported for use in lithium sulfur battery utilizing several different precursors. For example, using a mechanochemical approach and wood biomass with a mixture of melamine and urea along K_2CO_3 resulted in a high initial capacity of 1300 mAh g^{-1}.[45] In turn, using sugar cane bagasse as carbon source yielded initial specific capacity of 815 mAh g^{-1} and a capacity fading rate of 0.067% per cycle after 500 cycles, while demonstrating synergistic benefit of controlling the porous structure and doping with nitrogen.[46]

Wet chemistry synthesis is often favored for superior reaction and heat control compared to solid state synthesis, but commonly the used solvents restrict reaction temperatures to around 200 °C. As an alternative, use of molten inorganic salts as reaction medium can allow operation at temperatures over 1000 °C.[47] Molten salt synthesis has gained some popularity for producing functional carbons from biomass. At its simplest it consists of mixing the precursor with the selected salt, heating and finally removing the salt by washing.[48] Previously widely used for oxide ceramics production, it offers multiple benefits for synthesis of porous carbons, such as promotion of self-activation by the reactive gases formed in the reaction, increased yields and control of the product properties by changing the used salts, ratios and temperatures.[49] Simultaneous activation with LiCl/KCl molten salt system has been demonstrated to produce high surface area carbons with variety of morphologies depending on the selected activation agent.[50]

Despite the evidence indicating the feasibility of synthesizing high-porous micro- and mesoporous carbon with a desirable morphology from lignin, significant challenges persist in the utilization of biomass-based carbons in LiS batteries. The presence of a variety of structures in the carbon sources complicates the production of precisely controllable porous materials, and the chemical activation process often necessitates complex procedures and costly, highly corrosive reagents to yield high SSA materials. In order to address the aforementioned challenges, the present study proposes a novel approach that integrates the molten salt synthesis method with the activation of lignin by urea and potassium carbonate. This innovative method involves optimizing the porosity of the activated carbon and its morphology to enhance characteristics of synthesized material in LiS batteries. In this study, the softwood Kraft lignin was used as the carbon source to produce nitrogen doped oxygen containing porous carbon by combining eutectic KCl/NaCl molten salt (mp. 658 °C[47]) and urea/K_2CO_3 activation in a simple one-step process using affordable and environmentally benign raw materials. Molten salt was selected as the reaction medium as it has been found to function as a hard template below the melting point and the increased retention of volatiles, resulting in improved activation and yield.[49] In addition, KCl and K_2CO_3 also form eutectic solution further increasing activation.[51] Produced materials were extensively characterized, and sulfur composites and coin cells were prepared to assess electrochemical performance. Obtained in this study, desirable pore structure containing both micro- and mesopores combined with nitrogen and oxygen functional groups led to a high initial discharge capacity of 1407 mAh per g-S and capacity fade of 0.11%/cycle after 200 cycles at 0.2C rate.

2. Experimental

2.1. Synthesis of porous carbon materials

The eutectic salt mixture was prepared by carefully mixing potassium chloride (KCl, VWR Chemicals, analytical reagent

grade) and sodium chloride (NaCl, J.T. Baker, analytical reagent grade) together with a mass ratio of 44 to 56. In turn, softwood Kraft lignin (UPM Kymmene Oyj), urea ($CO(NH_2)_2$, ACS Merck, analytical reagent grade) and potassium carbonate (K_2CO_3, anhydrous, Fischer Chemicals, analytical reagent grade) were added to the salt mixture and carefully mixed until a homogeneous powder was obtained. For mixing the reagents, a mortar was used, and each sample was mixed for 10 minutes. Eight different carbon materials (CM) were prepared by altering the lignin to salt ratio, amounts of urea and K_2CO_3. Samples are denoted as CM *x-y-z* where *x*, *y* and *z* stand for mass of salt mixture, urea and potassium carbonate, compared to the mass of lignin, respectively. The amount of potassium carbonate was calculated based on the amount of urea according to eqn (1), with increases of 0.5 and 2 times the mass of lignin for samples with higher concentration. Table 1 presents a comprehensive overview of the utilized quantities of diverse components in the synthesis of mesoporous carbon from kraft lignin.

A mixture of urea and potassium carbonate was used for the activation of lignin to yield a high surface area and volume carbon host material. Urea reacts with potassium carbonate forming potassium cyanate and ammonium carbonate as described in reaction (1).[42] With heating, urea decomposes releasing ammonia and forming cyanuric acid, part of which in turn to CN radicals and NH_x that react with the carbon materials edge sites, resulting in nitrogen being incorporated into the material in heterocyclic structures.[42,52] Potassium carbonate then reacts with these nitrogen sites, producing KOCN and $-CO_2K$ as described in reaction (2). In turn, the $-CO_2K$ reacts, forming KOCN as described in reaction (3).[45,53] As the temperature rises, KOCN reacts with carbon, producing KCN and CO as described in reaction (4). The side products are easily removed with a simple washing step.[42]

$$CH_4N_2O + 0.5\ K_2CO_3 \rightarrow KOCN + 0.5\ (CH_8N_2O_3) \quad (1)$$

$$K_2CO_3 + C{-}N \rightarrow KOCN + {-}CO_2K \quad (2)$$

$$-CO_2K + C{-}N \rightarrow KOCN + CO \quad (3)$$

$$KOCN + C \rightarrow KCN + CO \quad (4)$$

Mixed reagents in an alumina crucible (Alsint) were heated in vertical tubular furnace under a nitrogen flow rate of 1 L min^{-1} to 800 °C using heating rate of 5 °C min^{-1} with 1 h holding time at 800 °C. Prior to heating the tube was flushed with nitrogen flow rate of 1 L min^{-1} for 20 min. After the heating, the sample was allowed to cool back down to room temperature before further processing. It should be noted that during the synthesis, a toxic side product KCN is formed in accordance with eqn (4).[42,54] To remove the remaining salt and synthesis byproducts, prepared material was washed with 1 M HCl (solution prepared from 37% HCl, Fisher chemicals, analytical reagent grade) for 2 h. This will lead to formation of toxic HCN gas, which can be collected by bubbling through NaOH solution to avoid its release.[55,56] The bubbling results in conversion to NaCN which can be further oxidized by addition of H_2O_2 to produce less harmful compounds.[57,58] The suspension was then vacuum filtrated, and the material was washed with ample amounts of deionized water (18.2 MΩ, Elga Maxima water purifier) until the pH of the filtrate was confirmed to be neutral. Afterwards, the material was dried at 80 °C overnight before further analysis.

Table 1 Parameters applied during synthesis of different sample: Mass ratios of molten salt, urea and K_2CO_3 to lignin

Sample name	Salt/Lignin (m m^{-1})	Urea/Lignin (m m^{-1})	K_2CO_3/Lignin (m m^{-1})
CM 0-4-5.1	0	4	5.1
CM 20-0-0	20	0	0
CM 20-1-1.7	20	1	1.7
CM 20-4-5.1	20	4	5.1
CM 20-4-4.6	20	4	4.6
CM 20-4-6.6	20	4	6.6
CM 10-4-5.1	10	4	5.1
CM 40-4-5.1	40	4	5.1

2.2. Preparation of the sulfur composite

For the preparation of porous carbon sulfur composite, a combination of chemical deposition and melt diffusion was selected to achieve even distribution of sulfur in the porous material. For the deposition, the produced carbon material and sodium thiosulfate ($Na_2S_2O_3{\cdot}(H_2O)_5$, Sigma-Aldrich, analytical reagent grade) were mixed in deionized water. Then, in a typical process, 1 M HCl was added dropwise to the solution under magnetic stirring to form sulfur particles. The sulfur mass percentage was calculated to be 70%. After 2 hours of mixing the active material composite was vacuum filtrated and washed with water several times until the filtrate was confirmed to have neutral pH value. The composite material was consequently dried at 80 °C overnight. For the following melt diffusion, the dried composite material was heated in nitrogen atmosphere at 155 °C overnight; this temperature allows sulfur to infiltrate the pores due to capillary action.

2.3. Characterization of materials

Thermogravimetric analysis (TGA) was conducted on TA Instruments Q50 TGA. Approximately 10 mg of the C/S composite material was weighed in a platinum pan. A ramp of 5 °C min^{-1} to maximum heating temperature of 450 °C was used with a N_2 purge flow of 90 mL min^{-1} for the sample and 10 mL min^{-1} for the balance.

N_2 adsorption and desorption for BET surface area analysis was conducted with MicroTrac BELSORP MAX X instrument at 77.35 K adsorption temperature. Samples were pretreated at 150 °C for 3 hours prior to the measurement. Pore volumes and size distributions were calculated based on the results in the following manner: for micropore (<2 nm) volume, the MP-method was used and for mesopore (2–50 nm) volume, NLDFT-calculation was used. For the NLDFT-calculation pores were assumed slit shaped, adsorbent selected to be graphitic carbon, Tikhonov regulation fitting was used, and solid and fluid pore width definition was selected. Average pore size was calculated with the BJH-method.

Scanning electron microscope (SEM) images were taken with a Zeiss SigmaHD VP FE-SEM, using a type II secondary electron

detector (SE2) detector and accelerating voltage of 10 keV. Energy-dispersive X-ray spectroscopy (EDS) analysis was conducted using Thermo Dual 60 mm^2 EDS SDD-detectors and accelerating voltages of 5 and 10 keV. Samples were prepared by mixing small amounts of carbon material in ethanol, applying the suspension to an aluminum stub (Agar Scientific), and allowing the solvent to evaporate prior to analysis.

The Raman spectra were measured using Thermo DxRzxi Raman Microscope using λ 532 nm laser, 10× objective, 50 μm confocal pinhole aperture, 2.5 mV laser power, 100 scans and exposure time of 0.25 s. For measurement the carbon material powders were applied to a microscope glass and slightly pressed to ensure sufficient adhesion.

Surface analysis of synthesized kraft lignin-based carbon samples was performed with X-Ray photoelectron spectrometer Thermo Fischer Nexsa G2 XPS, source gun X-Ray002 400 μm – FG ON. Survey scans were performed from –10 to 1350 eV with pass energy of 200 eV, 3 scans and 10 ms dwell time. Scans for C, N, O and S were performed from 279 to 298 eV, 392 to 410 eV, 525 to 545 eV and 157 to 175 eV respectively, with pass energy off 20 eV, 10 scans and 50 ms dwell time.

2.4. Electrochemical studies

Sulfur composites were used as active material for electrode creation. Prior to slurry preparation, the active material was sieved to 45 μm. Firstly, carboxymethyl cellulose (CMC) (Xiamen Tob New Energy Technology, purity 99.5%, viscosity 7000–10 000 mPa s (2% aqueous solution)) was dissolved in water, followed by the conductive material C65 (IMERYS, Ash content 0.025%, BET 62 $m^2\ g^{-1}$) and the active material. Finally, styrene butadiene rubber (SBR) binder (Xiamen Tob New Energy Technology, ∼48–53 wt% total solid, viscosity ∼50–250 mPa s) was added. The weight ratio of AM/C65/CMC/SBR was 80/15/2/3, respectively. After thorough mixing using both high speed magnetic stirring and ultrasound, the slurry was applied on a current collector (Xiamen Tob New Energy Technology, 16 μm aluminum foil) using doctor blade set to 130 μm wet coating thickness, if not specified otherwise, and then allowed to dry in room temperature. Prior to slurry application, the foil surface was cleaned of oxidation using acetone and ethanol. The electrodes were then cut into 14 mm diameter discs and further dried in a vacuum at 50 °C overnight prior to cell assembly, except for CM 20-0-0, for which no vacuum was used, as notable evaporation of sulfur was observed. The sulfur mass loading of the working electrodes, if not specified otherwise, was approximately 1 mg cm^{-2} with a total electrode mass of app. 8 mg.

For evaluation of electrochemical performance CR2016 coin cells were assembled in an argon filled glovebox with lithium foil as the anode, polypropylene separator (Celgard 2400, thickness 25 ± 2 μm, porosity 40 ± 5%) and electrolyte (1 M lithium bis(trifluoromethanesulfonyl) imide (LiTFSi) with 2 wt% lithium nitrate ($LiNO_3$) (Sigma-Aldrich) in 1.3-dioxolane (DOL) and dimethoxyethane (DME) (1 : 1 by volume) (Sigma-Aldrich)), in ratio 15 μL of per 1 mg of sulfur.

All electrochemical tests were performed using Arbin BTS battery test system. The formation cycling was performed at 0.1C discharge and charge rates, with 30 min dwell time in voltage window of 1.7 V to 2.8 V for 5 cycles. Cyclic voltammetry (CV) was carried out at a scan rate of 0.05 mV s^{-1} in voltage window of 1.7 to 2.8 V. Rate performance test was done by using 5 cycles at 0.1C, 0.2C, 0.5C, 1C and 2C for discharge currents and 0.2C charge current. Cycle life was tested for 200 cycles at 0.2C charge and discharge currents.

3. Results and discussion

3.1. Material properties

Scanning electron microscopy was utilized to assess the particle morphology of the created carbon materials. Images of materials CM 0-4-5.1, CM 20-0-0, CM 20-1-1.7 and CM 20-4-5.1 are presented in Fig. 1 showing a clear effect of molten salt and activation agents on the particle morphologies. The material CM 0-4-5.1, prepared only with urea and K_2CO_3 without molten salt, displays an irregular particle shape. Addition of molten salt clearly increases the size of the flakes (Fig. 1c), but without activation agents the molten salt (CM 20-0-0) results almost exclusively in thicker carbon flakes. The activated samples are more so a mixture of

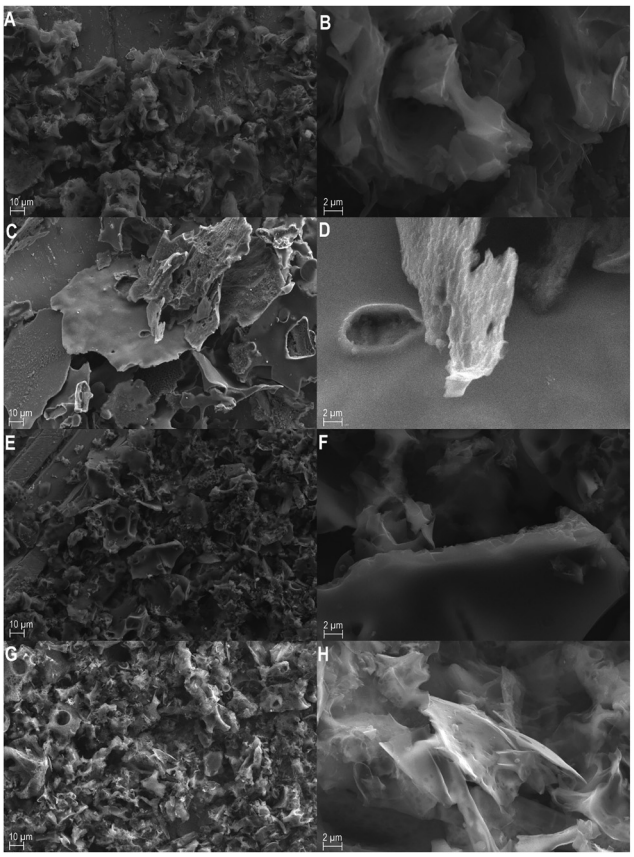

Fig. 1 SEM images at 3000× and 20 000× magnifications of the materials CM 0-4-5.1 (A and B), CM 20-0-0 (C and D), CM 20-1-1.7 (E and F) and and CM 20-4-5.1 (G and H). SE2 detector and 10 keV accelerating voltage were used.

Table 2 Yield of the carbon material, the ratio of intensities of disordered and graphitic Raman peaks (I_D/I_G), BET surface areas and micro and mesopore volumes and average pore diameters of the carbon materials. (*Type I (ISO 99277) used for determining BET)

Sample name	Yield (%)	I_D/I_G	BET surface area ($m^2\ g^{-1}$)	Mesopore volume ($cm^3\ g^{-1}$)	Micropore volume ($cm^3\ g^{-1}$)	Average pore diameter (nm)
CM 0-4-5.1	10	1.49	2564	0.840	1.396	2.33
CM 20-0-0	45	1.41	n.a.	n.a.	n.a.	n.a.
CM 20-1-1.7	42	1.37	2456*	0.183	1.154	1.58
CM 20-4-5.1	21	1.39	3125	1.003	1.697	2.28
CM 20-4-4.6	24	1.42	3122	0.984	1.690	2.25
CM 20-4-6.6	13	1.30	3081	1.011	1.667	2.29
CM 10-4-5.1	14	1.33	3249	1.238	1.815	2.51
CM 40-4-5.1	21	1.38	3423	0.946	1.786	2.12

morphologies in varying portions. CM 20-1-1.7 partially retains morphology like that of the non-activated sample, CM 20-4-5.1 in turn displays a more distorted particle shape, but upon closer inspection, thin, and sheetlike structures are observed. For the rest of the materials, no major differences were observed based on the SEM images (presented in the SI Fig. S1).

Product yields calculated as a percentage of the mass of lignin are presented in Table 2. Activation reduced the product yield notably as did further increasing potassium carbonate. The yield of the sample with molten salt was twice as much as the sample without molten salt. While the difference indicates less reaction takes place in the more dilute conditions, some of it could be attributed to the confining effect of the salt helping retain the volatile components. Previously, lower mass loss has been reported through the heating range when using molten salt.[59] Lowering the amount of salt resulted in lower yield, suggesting higher reactivity, but additionally, the amount may not have been enough to benefit from the possible retaining effect. Further increase of salt did not result in further increase in yield.

Surface analysis revealed that the activated materials had high specific surface areas, up to 3422 $m^2\ g^{-1}$ with the total pore volumes exceeding 2 $cm^3\ g^{-1}$. The results obtained are comparable to previous reports.[42] Sample CM 20-0-0 could not be successfully stabilized for measurement; however, surface area and pore volume are assumed to be low due to no activation and higher yield. Sample CM 20-1-1.7 was determined to be solely microporous, while others displayed type H4 hysteresis loop indicative of micro-mesoporous carbons.[60] Hysteresis and pore size distribution figures (both MP and NLDFT) are presented in SI (Fig. S2–S4). Reaction medium of molten salt appears to increase reactivity, as CM 0-4-5.1 exhibits the smallest surface area and porosity among the materials prepared with similar level of activation agents. This is in agreement with previous reports of KCl increasing reactivity between the carbon and K_2CO_3.[51,61] When no molten salt was used (sample CM 0-4-5.1), the lowest values for porosity and surface area among the materials with similar level of activation were obtained. The highest porosity was observed in sample CM 10-4-5.1, using the lowest amount of salt. Increasing the amount of molten salt led to decrease in pore volume and average pore diameter and increase in specific surface area. This can be explained by more dilute conditions leading to less activation taking place. Increasing the amount of potassium carbonate first slightly increased the total pore volume but further increases led to a slight decrease in SSA while the total pore volume remained the same. This is explained by further activation causing pores to combine to form larger pores. This is likewise demonstrated in CM 20-1-1.7 being almost entirely microporous, while an increase in the activating agents resulted in both higher microporosity and emergence of *meso*-porosity in CM 20-4-5.1.

For estimating graphitic content of the carbon materials, measured Raman spectra were deconvoluted in a typical fitting with four Gaussian curves.[62,63] Normalized spectra and example of deconvolution are presented in SI (Fig. S5). Deconvolution consists of D and G carbon peaks at 1350 and 1580 cm^{-1}, corresponding to sp^2 carbon, and peaks D3 and D4 at 1200 and 1500 cm^{-1}, respectively, corresponding to sp^3 carbon. The ratio of intensities for D/G peaks (I_D/I_G) was calculated based on the deconvolution, and the values are presented in Table 2, with higher value indicating more disordered structure and *vice versa*. The determination of values was achieved through the utilization of an average of ten points of measurement. The sample prepared without activation (CM 20-0-0) displayed higher I_D/I_G compared to activated materials. This is in part assumed to result from the higher amount of remaining surface oxygen functional groups. Molten salt appears to increase the formation of graphitic nanocrystals, as sample prepared without salt shows the most disordered structure. Molten salt systems have been shown to exhibit catalytic activity towards graphitization.[35] An increase in K_2CO_3 resulted in more graphitic structure. Potassium compounds have been reported to lower the graphitization temperature.[64] Additionally, this could be explained by the higher reactivity of amorphous carbon compared to graphitic carbon: despite K_2CO_3 activation producing defects, preferential consumption of amorphous regions results in remaining material displaying increased order.

Electron dispersive X-ray spectroscopy was applied to estimate the elemental composition of the prepared carbon materials. Estimates of the relative contents of carbon, oxygen, and sulfur are displayed in Table 3. Material appears to retain most sulfur when no activation agents are added. All samples display notable oxygen content, with activation slightly decreasing the weight percentage. As large carbon and oxygen peaks obstruct reliable determination of nitrogen *via* EDS analysis, samples

Table 3 Amounts of carbon, oxygen and sulfur as weight % based on the EDS spectral mapping and surface composition and weight percentages based on XPS measurement

	EDS			XPS				
Sample	C (w%)	O (w%)	S (w%)	C (w%)	O (w%)	N (w%)	Cl (w%)	S (w%)
CM 0-4-5.1	89.6	9.9	0.6	87.05	8.76	4.19	—	—
CM 20-0-0	87.7	10.2	2.1	83.31	13.74	0.67	1.35	0.94
CM 20-1-1.7	89.2	10.4	0.4	90.42	7.67	1.91	—	—
CM 20-4-5.1	88.6	9.8	1.5	87.94	8.8	3.26	—	—
CM 20-4-4.6	89.5	9.4	1.0					
CM 20-4-6.6	90.3	8.8	0.9					
CM 10-4-5.1	90.3	8.6	1.1					
CM 40-4-5.1	90.1	8.5	1.4					

CM 0-4-5.1, CM 20-0-0, CM 20-1-1.7 and CM 20-4-5.1 were selected for more detailed surface analysis using XPS. The spectrograms are presented in Fig. 2 and deconvolution of the peaks for sample CM 20-4-5.1 in Fig. 3. (Rest of element specific scans and deconvolutions are presented in the SI Fig. S6–S8). Surface compositions as mass percentage are presented in Table 3. Three main peaks are observed in the survey scans, C 1s at ∼285 eV, N 1s at ∼400 eV and O 1s at ∼533 eV. Narrow scan C 1s spectra shows shoulder peaks indicating presence of C–O, C═O and C–O═C bonds and π–π* satellite peak in addition to the carbon bonds C–C and C═C.[65] Narrow scan of O 1s spectra shows peaks consistent with C–O and C═O bonds.[66] Additionally peak of chemisorbed oxygen or adsorbed water is observed.[67] Narrow scan of N 1s reveals amine and imine groups with some oxidized nitrogen.[68] This is consistent with the use of urea as a nitrogen source. The results show that the addition of urea results in nitrogen doping of the material. An increase in urea resulted in a higher amount of nitrogen in the final product. Doping level can therefore be controlled to some extent using this synthesis method. While some sulfur is detected by the elemental scan for samples CM 0-4-5.1 and CM 20-0-0 the peak intensity is not high enough for chemically meaningful peak fitting.

Compared to EDS, XPS measurement shows higher oxygen content for sample CM 20-0-0 but lower oxygen content for the other samples. Differences between the EDS and XPS results are mainly explained by two factors: XPS scan observes only the material surface while EDS penetrates deeper into the bulk of

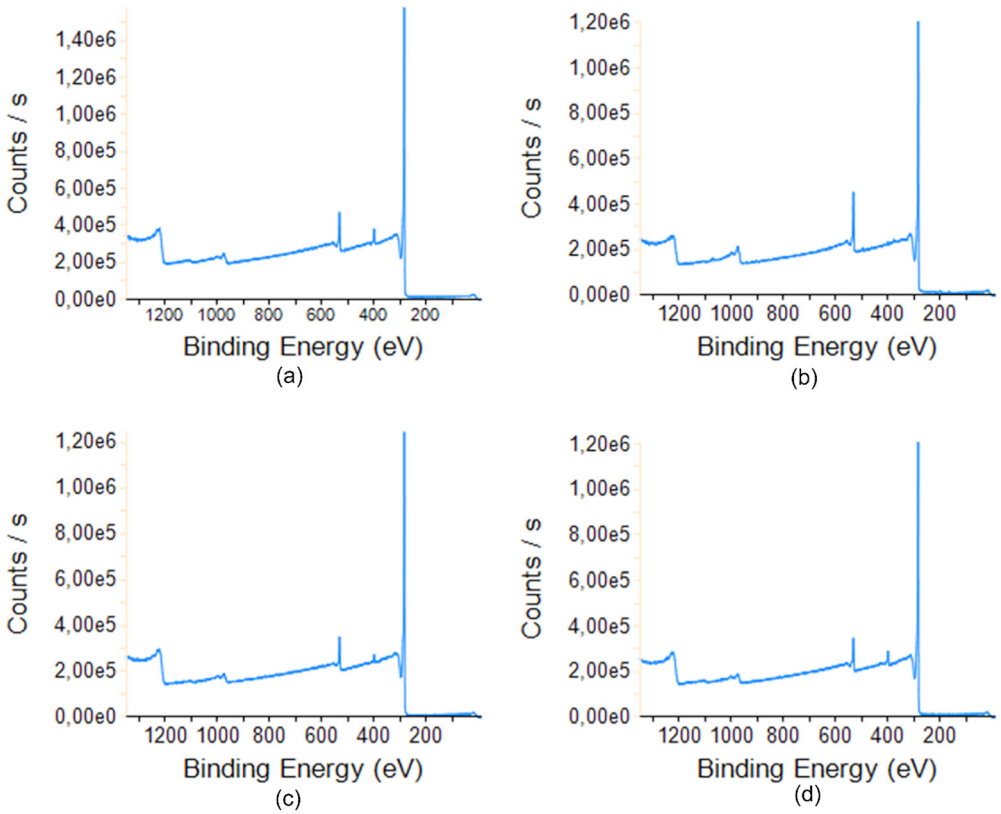

Fig. 2 XPS survey scans of samples (a) CM 0-4-5.1, (b) CM 20-0-0, (c) CM 20-1-1.7 and (d) CM 20-4-5.1. Scan range of −10 to 1350 eV, pass energy 200 eV and 3 scans with 10 ms dwell were used.

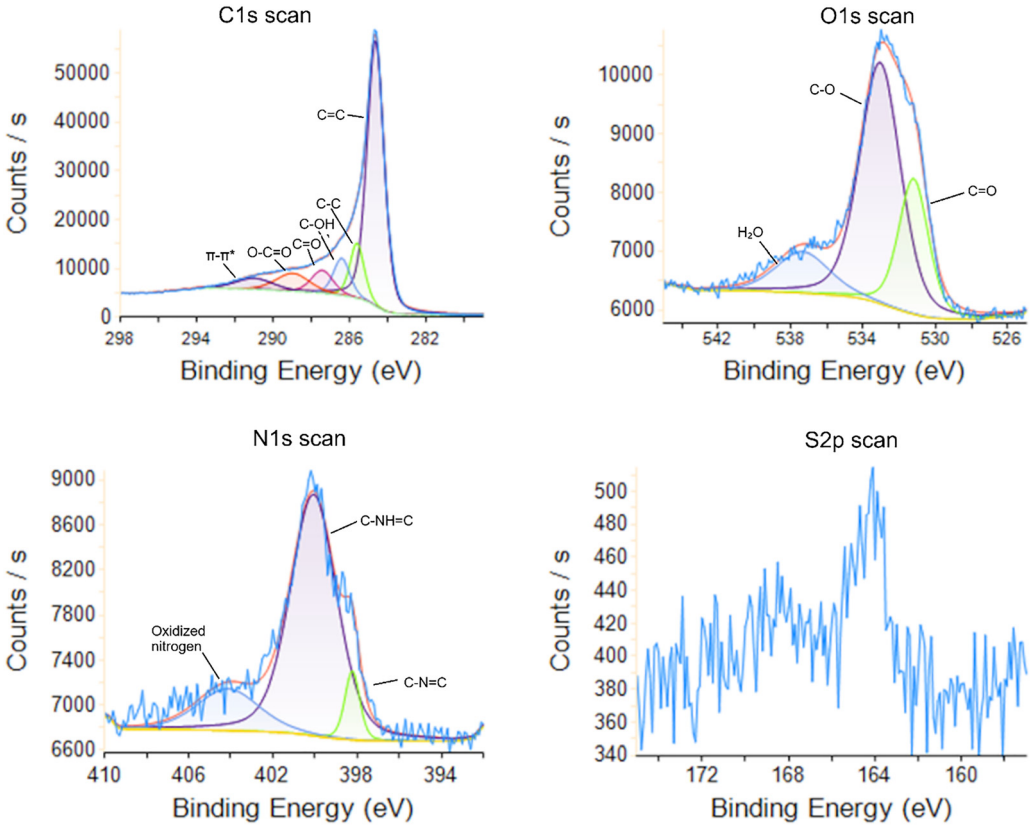

Fig. 3 Deconvoluted elemental scans of C, O, N and S for sample CM 20-4-5.1. Pass energy 20 eV, 10 scans and 50 ms dwell time were used.

the material and secondly, overlap of the oxygen and nitrogen peaks in EDS leads to some inaccuracy. Moreover, no sulfur was detected in the XPS scan, as seen in the figure of elemental scans of sample CM 20-4-5.1, except for a low amount of 0.9% in the sample CM 20-0-0. This means possible sulfur remaining in the other materials is in the bulk of the material and therefore does not affect the electrochemical performance. In sample CM 20-0-0, some Cl is also observed on the surface indicating the washing could not remove the salt completely in this case. Slightly higher amount of nitrogen is observed in case of no molten salt being used. This might be explained by better contact between urea and lignin when no salt is present.

3.2. Sulfur loading

TGA was performed on the prepared carbon sulfur composite materials to measure the actual sulfur content, and the data are presented in Fig. 4. The amount of sulfur in the composite is indicated by the mass loss (*S*% presented in Table 4).

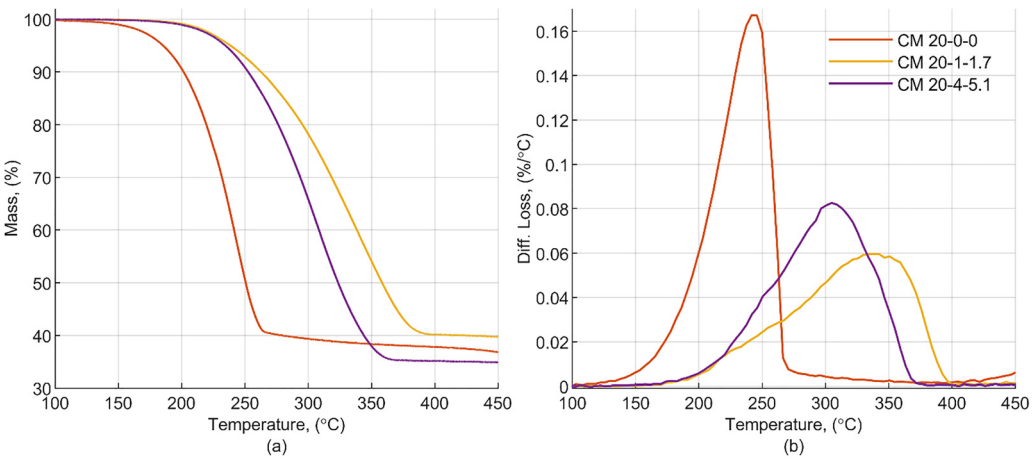

Fig. 4 TGA of the sulfur composites of materials prepared with different amounts of urea, (a) normalized weight as a function of the temperature and (b) the rate of weight change as a function of the temperature. Ramp rate of 5 °C min^{-1} under N_2 purge flow of 90 mL min^{-1}.

Table 4 Sulfur loading of the composites, mass loading of the electrodes and electrochemical performance of the LiS-coin cells

Sample name	Sulfur loading (wt%)	Mass loading (mg cm^{-2})	Initial coulombic efficiency (%)	Initial discharge capacity (mAh g^{-1})	Initial charge capacity (mAh g^{-1})	Average capacity fade after 200 cycles (%/cycle)
CM 0-4-5.1	60.6	1.37	92.6	1313	1215	0.173
CM 20-0-0	56.8	0.91	102.9	783	805	0.196
CM 20-1-1.7	59.2	0.99	101.5	830	841	0.267
CM 20-4-5.1	63.7	1.29	95.3	1220	1163	0.160
CM 20-4-4.6	63.6	1.34	92.9	1237	1149	0.164
CM 20-4-6.6	59.7	0.94	90.7	1407	1276	0.105
CM 10-4-5.1	61.3	1.21	92.5	1163	1075	0.095
CM 40-4-5.1	61.9	1.01	93.5	1232	1152	0.140

Composite sulfur loading varied from 56.8% of CM 20-0-0 to 63.7% of CM 20-4-4.6, variation in loading can be attributed to the structure of the carbon as the same amount of sulfur was used in all instances. Sulfur on the surface evaporates at a lower temperature while sulfur from the micropores requires a higher temperature to evaporate; therefore, a quick TGA measurement allows estimation of where the sulfur is in the composite. Plotting the derivate of mass as a function of temperature allows visualization of the position of sulfur after composite material creation.

The primary differences are observed when investigating materials prepared with different amounts of activation agents, as illustrated in Fig. 4. The sample without activation (CM 20-0-0) released sulfur at the lowest temperature, with a rate of mass loss peaking at 243 °C. The material with the mostly microporous structure, as observed by the BET measurement, (CM 20-1-1.7) required the highest temperature, reaching the greatest rate of mass loss at 336 °C.

When investigating materials prepared with different amounts of potassium carbonate, a slight shift in the peak temperature for mass loss is observed, with higher loading resulting in lower temperatures. Curves are presented in Fig. 5. The mass loss rate peaks at 296 °C for CM 20-4-6.6, while it peaks at 308 °C for CM 20-4-5.1.

When investigating materials prepared with different amounts of molten salt, it does not appear to exert a significant influence on the deposition of sulfur, as evidenced by Fig. 6. A higher peak mass loss temperature of 313 °C is observed for CM 0-4-5.1. For the remaining materials, only negligible variation is observed. The mass loss rate attains its maximum value at approximately 305 °C, suggesting comparable sulfur placement.

3.3. Electrochemical performances

The electrochemical performance of the different composites is presented in Table 4 and in Fig. 7–9. Initial coulombic efficiency was calculated as first de-lithiation/first lithiation, as lithium–sulfur cell is constructed in charged state and the first discharge commonly shows higher capacity than the first charge. Values exceeding 100% for samples CM 20-0-0 and CM 20-1-1.7 can likely be explained by self-discharging of the cells, as these materials also exhibit the fastest capacity decay indicating polysulfide shuttle is not adequately suppressed. Average capacity fade was calculated based on the cycling test; formation cycles were excluded.

When investigating materials prepared with different amounts of urea, as illustrated in Fig. 7, the greatest difference in performance is observed in samples CM 20-0-0 and CM 20-1-1.7, with no activation and lower level of activation, resulting in notably lower specific capacity attributable to poor sulfur utilization due to insufficient surface area and poor porosity. CM 20-0-0 and CM 20-1-1.7 display shifts in the observed peak locations compared to the other materials as well as lower peak currents. The shifts could be attributed to slower reaction

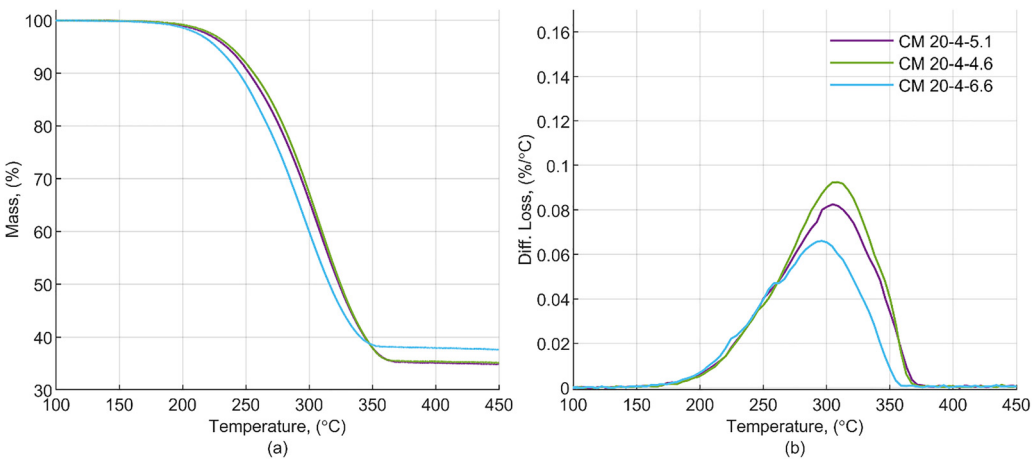

Fig. 5 TGA of the sulfur composites of materials prepared with different amounts of potassium carbonate, (a) normalized weight as a function of the temperature and (b) the rate of weight change as a function of the temperature. Ramp rate of 5 °C min^{-1} under N_2 purge flow of 90 mL min^{-1}.

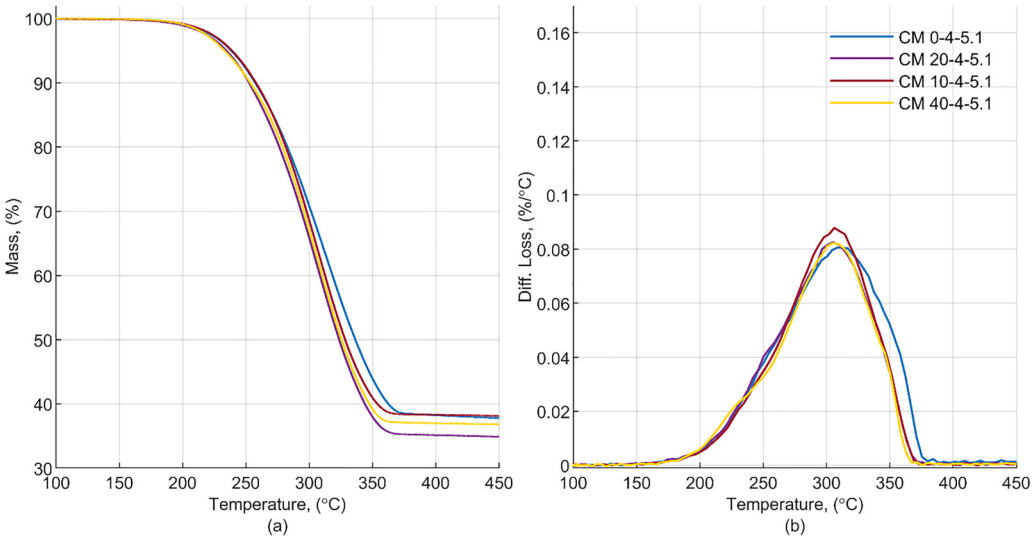

Fig. 6 TGA of the sulfur composites of materials prepared with different amounts of molten salt, (a) normalized weight as a function of the temperature and (b) the rate of weight change as a function of the temperature. Ramp rate of 5 °C min^{-1} under N_2 purge flow of 90 mL min^{-1}.

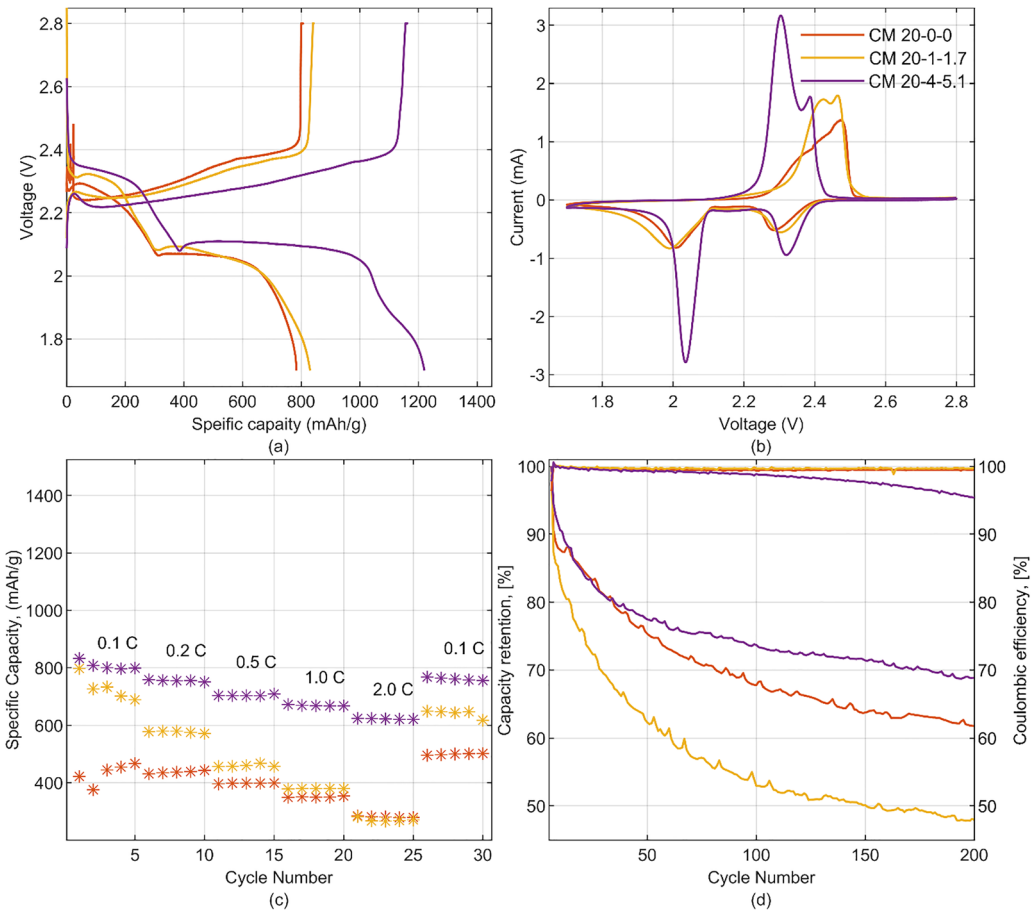

Fig. 7 Electrochemical test of the samples CM 20-0-0, CM 20-1-1.7 and CM 20-4-5.1, investigating materials prepared with different amounts of urea. (a) Formation at 0.1C, (b) cyclic voltammetry at 0.05 mV s^{-1}, (c) current rate (0.2C charge current) and (d) cycle life tests at 0.2C. Electrolyte: 1 M LiTFSi with 2 wt% ($LiNO_3$) in 1 : 1 DOL/DME, 15 μL/1 mg of sulfur.

kinetics on the discharge and oxidation resistance in the charging caused for example by insufficient reaction surface. The material with solely microporous structure displayed the fastest capacity decay, maintaining only 48% of capacity after

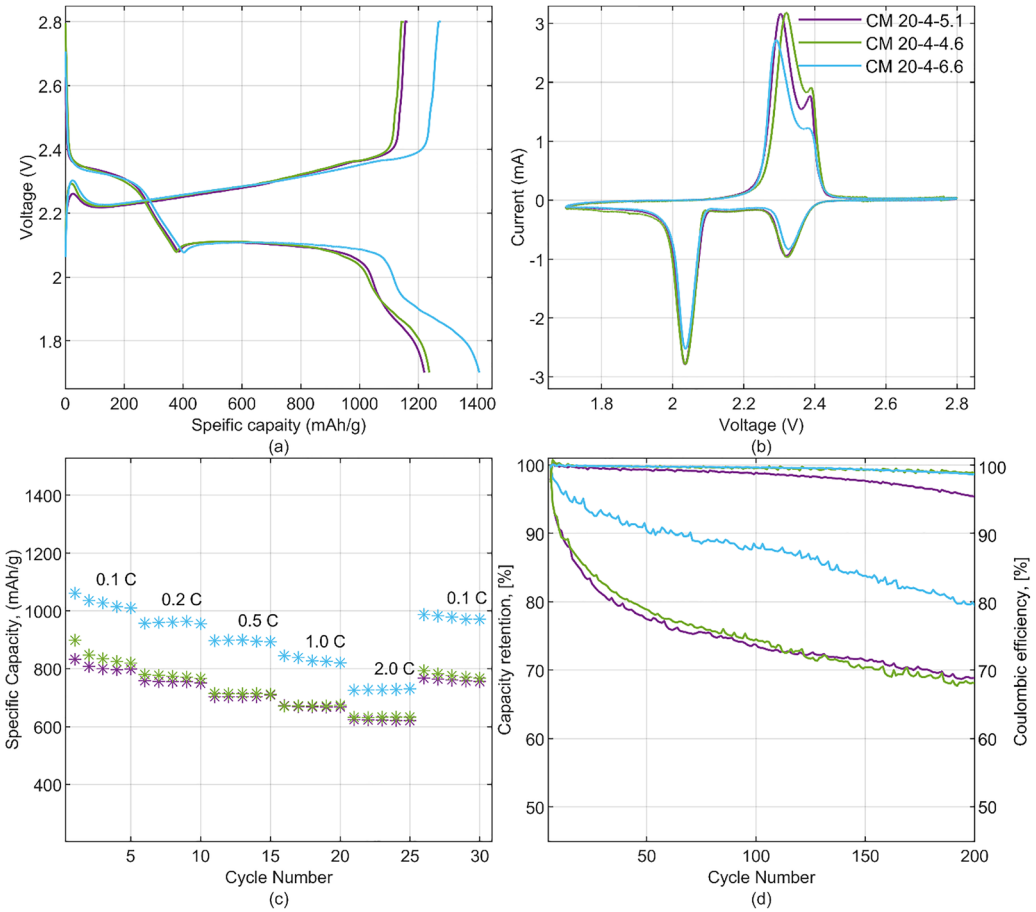

Fig. 8 Electrochemical test of the samples CM 20-4-5.1, CM 20-4-4.6 and CM 20-4-6.6, investigating materials prepared with different amounts of potassium carbonate. (a) Formation at 0.1C, (b) cyclic voltammetry at 0.05 mV s^{-1}, (c) current rate (0.2C charge current) and (d) cycle life tests at 0.2C. Electrolyte: 1 M LiTFSi with 2 wt% ($LiNO_3$) in 1 : 1 DOL/DME, 15 μL/1 mg of sulfur.

200 cycles. Previously, both too high and too low micropore content have been reported to reduce stability and initial specific capacity, mostly due to poor sulfur utilization and the shuttle effect.[69] Additionally, small pore size has also been reported to limit the electrolyte penetration leading to slower kinetics.[70] Another explanation for the poor cycling stability using microporous material suggested in the literature is that the pores can get blocked by lithium sulfide and the expansion can cause fractures in the material.[71]

When investigating materials prepared with different amounts of potassium carbonate, increasing the amount resulted in notably improved electrochemical performance as shown in Fig. 8. Mesoporous carbons have been reported to offer more ion transport pathways and to ensure good contact with the electrolyte.[10] Sample CM 20-4-6.6 displays the highest specific capacity of 1407 mAh per g-S, 83% of the theoretical capacity of sulfur. This performance is attributed to the favorable pore structure contributing to higher sulfur utilization. Notable increase in initial specific capacity, enhanced rate performance and improved capacity retention compared to CM 20-4-5.1 and CM 20-4-4.6 are observed. Based on the CV curve, the increase of K_2CO_3 also slightly improved kinetics, evidenced by lower oxidation potential.

When investigating materials prepared with different amounts of molten salt, in Fig. 9, CM 0-4-5.1 with no molten salt displays the highest initial capacity and improved rate performance reaching 838 mAh per g-S at 2C current, which can likely be partly attributed to the higher level of nitrogen doping revealed by the XPS analysis. Suitable nitrogen content has been previously reported to greatly improve conductivity of the carbon material and better adsorption of the polysulfides can also contribute to greater sulfur utilization.[37] Cycling performance in turn is not so favorable as only 66% of capacity is retained after 200 cycles compared to 81% of CM 10-4-5.1. The improved stability in the case of CM 10-4-5.1 can likely be attributed to higher pore volume as revealed by the BET analysis. Electrochemical performance has been reported to benefit from partial sulfur loading as it improves contact between sulfur and the carbon host.[72] In the case of CM 10-4-5.1 rate performance test was terminated prematurely due to cell malfunction, measured values are presented, and performance can be estimated as most cycles were completed.

The effect of the sulfur mass loading on electrochemical performances was investigated of the example of the material possessing the best performances. Two more electrodes were prepared from CM 20-4-6.6 with sulfur loading ratios 2.62 and

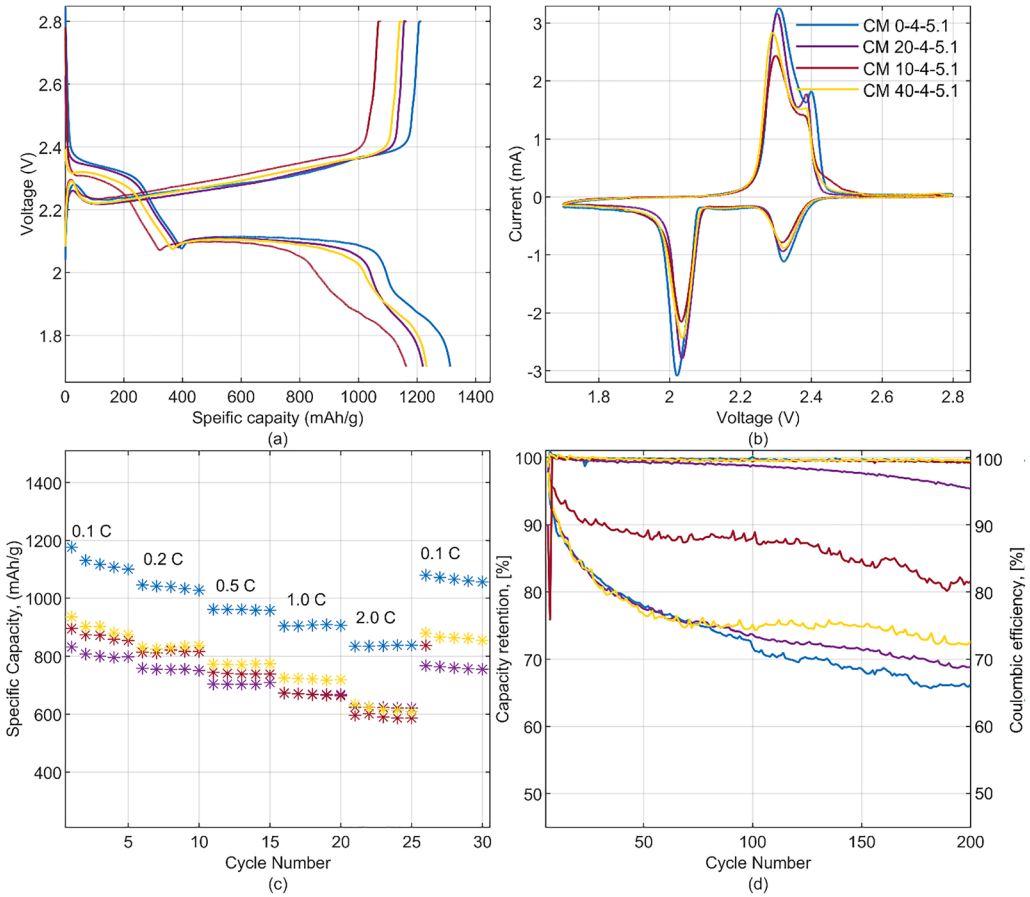

Fig. 9 Electrochemical test of the samples CM 0-4-5.1, CM 20-4-5.1, CM 10-4-5.1 and CM 40-4-5.1, investigating materials prepared with different amounts of molten salt. (a) Formation at 0.1C, (b) cyclic voltammetry at 0.05 mV s^{-1}, (c) current rate (0.2C charge current) and (d) cycle life tests at 0.2C. Electrolyte: 1 M LiTFSi with 2 wt% ($LiNO_3$) in 1 : 1 DOL/DME, 15 μL/1 mg of sulfur.

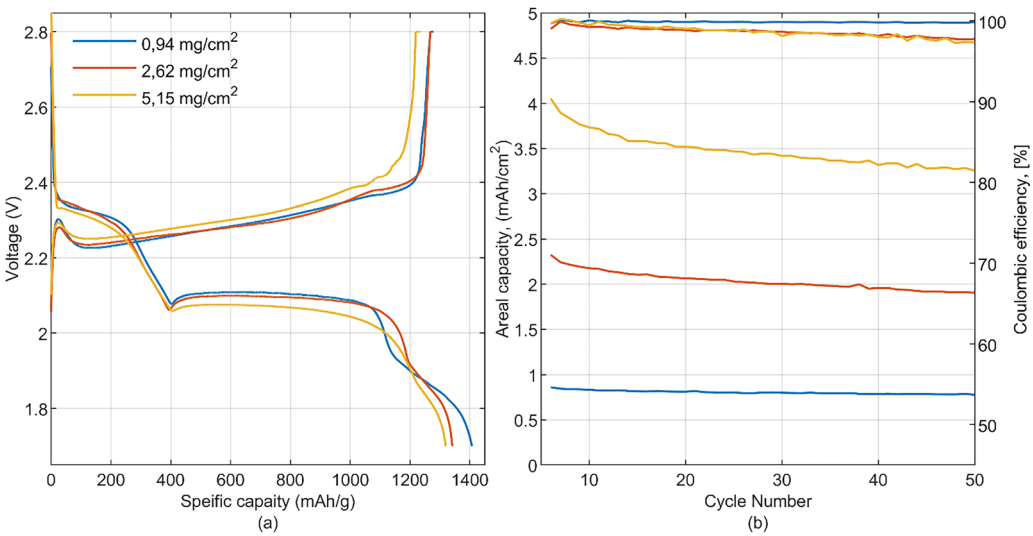

Fig. 10 Formation cycle and cycle life testing of material CM 20-4-6.6 with sulfur loading ratios of 0.94, 2.62 and 5.15 mg cm^{-2}. (a) Formation at 0.1C, (b) cycle life tests at 0.2C, (0.1C for the 5,15 mg cm^{-2}). Electrolyte: 1 M LiTFSi with 2 wt% ($LiNO_3$) in 1 : 1 DOL/DME, 15 μL/1 mg of sulfur.

5.15 mg cm^{-2}, using same electrolyte to sulfur ratio (E/S) of 15 μL mg^{-1} to obtain comparable results. While mass loading of approximately 1–2 mg cm^{-2} is generally recommended to enable comparisons between different studies, for practical

results sulfur loading of 5 mg cm^{-2} should be exceeded.[73,74] Ideally host material would be highly conductive, catalytically active and display good performance at a high sulfur content (>70%) and low E/S ratio (<5 μL mg^{-1}).[75] Formation cycle and cycle life testing displaying the development of areal capacity are presented in Fig. 10. For the 5.15 mg cm^{-2} cell the charging rate for cycle life testing was reduced to 0.1C to avoid issues with the lithium foil. A slight decline in electrochemical performance was observed with increasing sulfur mass loading ratio. This decline could likely be attributable to a reduction in electrode wettability. However, the 5.15 mg cm^{-2} electrode demonstrated a high initial specific capacity and, more notably, an area-specific capacity initially exceeding 4 mAh cm^{-2} and maintaining 3.25 mAh cm^{-2} after 50 cycles. The areal capacity is comparable to ultra-high mass loading commercial lithium-ion cathodes (typically 3–4 mAh cm^{-2}).[72] The results obtained from this study indicate that proper optimization of the porosity together with nitrogen doping is a viable method for creating an electrode for Li–Sulfur batteries that exhibits commercially attractive properties.

4. Conclusions

In this study, porous nitrogen-doped carbon materials were produced from Kraft lignin by utilizing NaCl/KCl mixture molten salt synthesis and urea/K_2CO_3 activation in a simple, single synthesis step. Increasing the level of activation had a notable effect on the carbon yield, porosity, and the electrochemical properties. At lower level of activation microporous material was produced, but this material displayed poor cycling stability. Increasing the amount of activation agents introduced mesopores to the material resulting in improved sulfur utilization and electrochemical performance. The molten salt medium was demonstrated to have a positive effect on product yield, porosity, and graphitization. As a result, materials with comparable level of activation prepared using molten salt displayed improved cycling stability compared to the material prepared without the molten salt. Increasing the amount of K_2CO_3 increased both *meso*-porosity and graphitization in the material. This, in turn, enhanced electrochemical performance. Nitrogen doping and variations in oxygen content were confirmed in the produced materials; it is acknowledged that optimization of the levels ought to be conducted to further increase performance. Material with highest detected nitrogen content showed the best rate performance. The overall best created composite material showed good initial specific capacity (1407 mAh per g-S), high coulombic efficiency, relatively good rate performance and cycling stability. In addition, the material exhibited satisfactory performance at commercially viable mass loading levels.

Author contributions

Juhana Jämsén: conceptualization, investigation, visualization and writing – original draft. Pauliina Nevalainen: investigation, formal analysis and writing – review & editing. Anna Lähde: writing – review & editing. Kirill Murashko: conceptualization, investigation, funding acquisition, supervision and writing – review & editing.

Conflicts of interest

There are no conflicts to declare.

Data availability

Data for this article, including images, spectra and the electrochemical testing data are available at zenodo.org at https://doi.org/10.5281/zenodo.16924551.

The data supporting this article, such as graphs and spectra, have been included as part of the supplementary information (SI). Supplementary information is available. See DOI: https://doi.org/10.1039/d5ya00266d.

Acknowledgements

Authors acknowledge Jane and Aatos Erkko Foundation for research funding 2023-2026 (University of Eastern Finland, AeroLiS-project (grant number 230018)).

References

1 S. Evers and L. F. Nazar, *Acc. Chem. Res.*, 2013, **46**, 1135–1143.
2 *Global EV Outlook 2024 – Analysis - IEA*, https://www.iea.org/reports/global-ev-outlook-2024, (accessed 14 March 2025).
3 C. Kongklaew, K. Phoungthong, C. Prabpayak, M. S. Chowdhury, I. Khan, N. Yuangyai, C. Yuangyai and K. Techato, *Sustainability*, 2021, **13**, 12839.
4 A. Pamidimukkala, S. Kermanshachi, J. M. Rosenberger and G. Hladik, *Transp. Res. Interdiscip. Perspect.*, 2023, **22**, 100962.
5 S. Bobba, S. Carrara, J. Huisman, F. Mathieux and C. Pavel, *Critical Raw Materials for Strategic Technologies and Sectors in the EU – a Foresight Study*, 2020.
6 H. Danuta and U. Juliusz, *US Pat.*, US3043896A, 1958.
7 J. Liang, Z. H. Sun, F. Li and H. M. Cheng, *Energy Storage Mater.*, 2016, **2**, 76–106.
8 Z. Zheng, G. Xia, J. Ye, Z. Fu, X. Li, M. J. Biggs and C. Hu, *Lithium-Sulfur Batteries: Materials, Challenges and Applications*, 2022, pp. 603–626.
9 H. Zhang, X. Li and H. Zhang, *Li-S and Li-O_2 Batteries with High Specific Energy,* Springer Singapore, Singapore, 2017.
10 S. Tiwari, V. Yadav, A. K. Poonia and D. Pal, *J. Energy Storage*, 2024, **94**, 112347.
11 X. He, J. Ren, L. Wang, W. Pu, C. Jiang and C. Wan, *J. Power Sources*, 2009, **190**, 154–156.
12 R. Demir-Cakan, *Li-S Batteries: The Challenges, Chemistry, Materials and Future Perspectives*, 2017, pp. 1–30.

13 D. Aurbach, E. Zinigrad, H. Teller and P. Dan, *J. Electrochem. Soc.*, 2000, **147**, 1274.
14 M. Wang, X. Xia, Y. Zhong, J. Wu, R. Xu, Z. Yao, D. Wang, W. Tang, X. Wang and J. Tu, *Chem. – Eur. J.*, 2019, **25**, 3710–3725.
15 H. Marsh and F. Rodríguez-Reinoso, *Act. Carbon*, 2006, 1–536.
16 Q. Li, Y. Liu, Y. Wang, Y. Chen, X. Guo, Z. Wu and B. Zhong, *Ionics*, 2020, **26**, 4765–4781.
17 D. S. Argyropoulos and S. B. Menachem, in *Biotechnology in the Pulp and Paper Industry*, ed K. E. L. Eriksson, *et al.*, Springer, Berlin, Heidelberg, 1997, pp. 127–158.
18 M. T. Munir, M. Naqvi, B. Li, R. Raza, A. Khan, S. A. A. Taqvi and A. S. Nizami, *J. Energy Storage*, 2024, **82**, 110477.
19 H. Wang, F. Fu, M. Huang, Y. Feng, D. Han, Y. Xi, W. Xiong, D. Yang and L. Niu, *Nano Mater. Sci.*, 2023, **5**, 141–160.
20 A. Beaucamp, M. Muddasar, I. S. Amiinu, M. Moraes Leite, M. Culebras, K. Latha, M. C. Gutiérrez, D. Rodriguez-Padron, F. del Monte, T. Kennedy, K. M. Ryan, R. Luque, M. M. Titirici and M. N. Collins, *Green Chem.*, 2022, **24**, 8193–8226.
21 W. J. Chen, C. X. Zhao, B. Q. Li, T. Q. Yuan and Q. Zhang, *Green Chem.*, 2022, **24**, 565–584.
22 P. Li, S. Wu and Y. Ding, *BioResources*, 2024, 3979–4000.
23 Z. Zhang, S. Yi, Y. Wei, H. Bian, R. Wang and Y. Min, *Polymers*, 2019, **11**, 1946.
24 Z. Chen, M. Lu, Y. Qian, Y. Yang, J. Liu, Z. Lin, D. Yang, J. Lu and X. Qiu, *Adv. Energy Mater.*, 2023, **13**, 2300092.
25 X. Sun, M. Chen, Z. Lin, Q. Wang, Y. Zhao, H. Wang, W. Wang and Y. Huang, *Int. J. Biol. Macromol.*, 2025, **305**, 141279.
26 C. Guizani, O. Sorsa, V. Siipola, T. Ohra-Aho, R. Paalijärvi, A. Pasanen, M. Mäkelä, A. Kalliola, M. Vilkman and K. Torvinen, *Biomass Convers. Biorefin.*, 2024, **14**, 21149–21163.
27 S. Zhou, Y. Xue, A. Sharma and X. Bai, *ACS Sustainable Chem. Eng.*, 2016, **4**, 6608–6617.
28 H. Yang, R. Yan, H. Chen, D. H. Lee and C. Zheng, *Fuel*, 2007, **86**, 1781–1788.
29 D. Robertson, P. Nousiainen, L. Pitkänen, I. Schlapp-Hackl, D. Rusakov and M. Hummel, *J. Anal. Appl. Pyrolysis*, 2024, **183**, 106811.
30 W. Li and J. Shi, *Front. Bioeng. Biotechnol.*, 2023, **11**, 1121027.
31 T. Z. Hou, X. Chen, H. J. Peng, J. Q. Huang, B. Q. Li, Q. Zhang and B. Li, *Small*, 2016, **12**, 3283–3291.
32 J. P. Paraknowitsch and A. Thomas, *Energy Environ. Sci.*, 2013, **6**, 2839–2855.
33 J. Wang and W. Q. Han, *Adv. Funct. Mater.*, 2022, **32**, 2107166.
34 S. S. Zhang, *Inorg. Chem. Front.*, 2015, **2**, 1059–1069.
35 Y. Chen, Y. Liao, Y. Qing, Y. Ding, Y. Wu, L. Li, S. Luo and Y. Wu, *J. Energy Storage*, 2024, **99**, 113186.
36 L. Yoshida, T. Hakari, Y. Matsui, Y. Orikasa and M. Ishikawa, *ACS Appl. Mater. Interfaces*, 2025, **17**, 22822–22830.
37 F. Sun, J. Wang, H. Chen, W. Li, W. Qiao, D. Long and L. Ling, *ACS Appl. Mater. Interfaces*, 2013, **5**, 5630–5638.
38 H. Chen, Y. Wei, J. Wang, W. Qiao, L. Ling and D. Long, *ACS Appl. Mater. Interfaces*, 2015, **7**, 21188–21197.
39 Y. Zhao, Z. Wang, X. Zhao, X. Wang, K. H. Lam, F. Chen, L. Zhao, S. Wang and X. Hou, *Energy Fuels*, 2020, **34**, 10188–10195.
40 X. G. Sun, X. Wang, R. T. Mayes and S. Dai, *ChemSusChem*, 2012, **5**, 2079–2085.
41 X. Li and X. Sun, *Front. Energy Res.*, 2014, **2**, 116949.
42 N. Tsubouchi, M. Nishio and Y. Mochizuki, *Appl. Surf. Sci.*, 2016, **371**, 301–306.
43 A. B. Fuertes and M. Sevilla, *Carbon*, 2015, **94**, 41–52.
44 A. B. Fuertes and M. Sevilla, *ChemSusChem*, 2015, **8**, 1049–1057.
45 J. Yaokawa, K. Oikawa and K. Anzai, *Calphad*, 2007, **31**, 155–163.
46 S. Wang, K. Zou, Y. Qian, Y. Deng, L. Zhang and G. Chen, *Carbon*, 2019, **144**, 745–755.
47 X. Liu, N. Fechler and M. Antonietti, *Chem. Soc. Rev.*, 2013, **42**, 8237–8265.
48 I. L. Egun, H. He, D. Hu and G. Z. Chen, *Adv. Sustainable Syst.*, 2022, **6**, 2200294.
49 N. Díez, A. B. Fuertes and M. Sevilla, *Energy Storage Mater.*, 2021, **38**, 50–69.
50 X. Liu and M. Antonietti, *Carbon*, 2014, **69**, 460–466.
51 M. Sevilla, N. Díez and A. B. Fuertes, *ChemSusChem*, 2021, **14**, 94–117.
52 E. Kasai, S. Kuzuhara, H. Goto and T. Murakami, *ISIJ Int.*, 2008, **48**, 1305–1310.
53 S. R. Kelemen, M. L. Gorbaty and P. J. Kwiatek, *Energy Fuels*, 1994, **8**, 896–906.
54 C. Jia, J. Luo, J. Fan, J. H. Clark, S. Zhang and X. Zhu, *J. Environ. Sci.*, 2021, **100**, 250–256.
55 V. Kyoseva, E. Todorova and I. Dombalov, *J. Univ. Chem. Technol. Metall.*, 2009, **44**, 403–408.
56 M. Sevilla, G. A. Ferrero, N. Diez and A. B. Fuertes, *Carbon*, 2018, **131**, 193–200.
57 W. John, *Williams, Handbook of anion determination*, Butterworths, 1984, vol. 71.
58 D. Pak and W. Chang, *Environ. Technol.*, 1997, **18**, 557–561.
59 C. Wang, D. Wu, H. Wang, Z. Gao, F. Xu and K. Jiang, *J. Mater. Chem. A*, 2018, **6**, 1244–1254.
60 M. Thommes, K. Kaneko, A. V. Neimark, J. P. Olivier, F. Rodriguez-Reinoso, J. Rouquerol and K. S. W. Sing, *IUPAC Technical Report Physisorption of gases, with special reference to the evaluation of surface area and pore size distribution (IUPAC Technical Report)*, 2015.
61 N. Díez, G. A. Ferrero, M. Sevilla and A. B. Fuertes, *J. Mater. Chem. A*, 2019, **7**, 14280–14290.
62 *GitHub - MacDumi/RAMAN-Deconvolution: Deconvolution of Raman spectra*, https://github.com/MacDumi/RAMAN-Deconvolution, (accessed 5 November 2024).
63 A. Ferrari and J. Robertson, *Phys. Rev. B: Condens. Matter Mater. Phys.*, 2000, **61**, 14095.
64 V. Pusarapu, R. Narayana Sarma, P. Ochonma and G. Gadikota, *npj Mater. Sustainability*, 2024, **2**, 16.
65 M. C. Biesinger, *Appl. Surf. Sci.*, 2022, **597**, 153681.
66 High Resolution XPS of Organic Polymers: The Scienta ESCA300 Database (Beamson, G.; Briggs, D.), Division of Chemical Education, 1993, **vol. 70**.

67 S. D. Gardner, C. S. K. Singamsetty, G. L. Booth, G. R. He and C. U. Pittman, *Carbon*, 1995, **33**, 587–595.
68 C. M. Goodwin, Z. E. Voras, X. Tong and T. P. Beebe, *Coatings*, 2020, **10**, 1–12.
69 P. Wu, L. H. Chen, S. S. Xiao, S. Yu, Z. Wang, Y. Li and B. L. Su, *Nanoscale*, 2018, **10**, 11861–11868.
70 Z. Hu, C. Geng, L. Wang, W. Lv and Q. H. Yang, *Adv. Energy Sustainability Res.*, 2024, **5**, 2300148.
71 P. Barai, A. Mistry and P. P. Mukherjee, *Extreme Mech. Lett.*, 2016, **9**, 359–370.
72 X. Li, Y. Cao, W. Qi, L. V. Saraf, J. Xiao, Z. Nie, J. Mietek, J. G. Zhang, B. Schwenzer and J. Liu, *J. Mater. Chem.*, 2011, **21**, 16603–16610.
73 A. Bhargav, J. He, A. Gupta and A. Manthiram, *Joule*, 2020, **4**, 285–291.
74 S. Yari, A. Conde Reis, Q. Pang and M. Safari, *Nat. Commun.*, 2025, **16**, 1–15.
75 F. Wang, Y. Han, X. Feng, R. Xu, A. Li, T. Wang, M. Deng, C. Tong, J. Li and Z. Wei, *Int. J. Mol. Sci.*, 2023, **24**, 7291.